7.6 High-resolution simulations of downslope flows over complex terrain using WRF-IBM

Robert S. Arthur[1,*], Katherine A. Lundquist[2], Jeffrey D. Mirocha[2], Sebastian W. Hoch[3], and Fotini K. Chow[1]

[1]Department of Civil & Environmental Engineering, University of California, Berkeley, CA
[*]Corresponding author email address: barthur@berkeley.edu
[2]Lawrence Livermore National Laboratory, Livermore, CA
[3]Department of Atmospheric Sciences, University of Utah, Salt Lake City, UT

Abstract

In this work, the evening transition to downslope flow on a mountain slope is examined using the Weather Research and Forecasting (WRF) model. The case study is Granite Mountain, Utah, which was the site of the Mountain Terrain Atmospheric Modeling and Observations (MATERHORN) project. Due to the steep topography of Granite Mountain, an immersed boundary method (IBM) is employed. IBM was implemented into the WRF model by Lundquist *et al.* (2010, 2012) and removes the restrictions on terrain slope that are associated with WRF's traditional terrain-following vertical coordinate. Idealized flow over Granite Mountain is simulated with 50 m horizontal resolution and approximately 10 m vertical resolution near the surface with no-slip bottom boundary conditions. The forcing in the model comes from the incoming solar radiation, including slope and topographic shading effects, and realistic land-use and soil-type data are included. Model results suggest that the location and timing of downslope flow development on the east slope of Granite Mountain depend strongly on topographic shading. Furthermore, seasonal differences in shadow propagation and soil moisture affect downslope flow development. Qualitative agreement is found between model results and observed data from several intensive observation periods (IOPs) during the MATERHORN field campaign.

---

1 Introduction

Thermally-driven slope flows are ubiquitous in mountainous terrain, and are important contributors to local weather. Such flows are generally characterized as either upslope or downslope, and develop due to heat exchange between the surface and the near-surface air. When the surface is heated by incoming solar radiation, the near-surface air becomes warmer than air at the same altitude away from the slope, giving it positive buoyancy and causing it to flow upslope. Alternatively when the ground cools, the near-surface air cools as well, giving it negative buoyancy and causing it to flow downslope. Slope flows vary diurnally with two transition periods, the "morning transition" from downslope flows at night to upslope flows during the day, and the "evening transition" from upslope flows during the day to downslope flows at night.

Diurnal mountain wind systems are thoroughly reviewed by Zardi & Whiteman (2013). They define upslope and downslope flows as thermally-driven diurnal winds that develop on valley sidewalls or isolated mountains, with upslope flows occurring during the day and downslope flows occurring at night. Upslope and downslope flows are distinguished from anabatic and katabatic flows, which refer more generally to flows that move up and down the terrain and are not necessarily diurnal or thermally-driven. The term "katabatic" is also used to refer to large-scale flows over Antarctica and Greenland that are affected by the Coriolis force. Furthermore, Zardi & Whiteman (2013) distinguish upslope and downslope flows from up-valley and down-valley flows, which occur on a larger scale along the major axis of valleys. The convention of Zardi & Whiteman (2013) is followed here, and analysis is focused on the evening transition to downslope flows on an isolated mountain.

The classic analytical model for downslope flow was presented by Prandtl (1942). In this steady-state model, the downslope advection of buoyancy is balanced by slope-normal turbulent diffusion of buoyancy, while the downslope acceleration due to gravity is balanced by slope-normal turbulent diffusion of momentum. Prandtl's (1942) model captures the jet-like structure of the downslope velocity profile, where the maximum velocity occurs at some height above the sloping bottom. Many studies have since have updated the Prandtl (1942) model to more accurately represent field observations. Modifications include height-variable turbulent diffusivities (Grisogono & Oerlemans, 2001), time-dependence (Grisogono, 2003), and Coriolis effects (Gutman & Malbakhov, 1964; Stiperski *et al.*, 2007; Kavčič & Grisogono, 2007; Shapiro & Fedorovich, 2008).

In addition to steady-state analytical models of downslope flows, there are several analytical models for the development of downslope flows during the evening transition. Two particular models, the "cooling slab" and the "front formation" models, are discussed and illustrated by Fernando *et al.* (2013). In both models, uniform surface cooling is imposed on an upslope flow on a simple slope. In the cooling slab model, dense air builds up near the surface until the downslope buoyancy force can overcome frictional forces, causing the downslope flow to develop along the entire slope simultaneously. In the front model, developed by Hunt *et al.* (2003), the cooling of near-surface air parcels depends on their initial position and velocity, and therefore does not occur simultaneously along the entire slope. Instead, a stagnation front develops where air parcels reach a balance between their upslope inertia and the downslope buoyancy force. This front moves gradually down the slope, causing the developing downslope flow to "undercut" the remaining upslope flow.

Numerical modeling of katabatic flows has occurred at a range of physical scales, as is thoroughly reviewed by Axelsen & van Dop (2009). Mesoscale models have been used to study realistic katabatic flows, while large-eddy simulations (LES) have been used to study katabatic flows at higher resolutions under idealized conditions (e.g., Skyllingstad, 2003, who used constant surface cooling and a uniform slope). Additionally, Smith & Skyllingstad (2005) used LES to explore the effect of a nonuniform slope on katabatic flows, while Smith & Porté-Agel (2014) explored the effect of various subgrid models. A primary challenge associated with LES of downslope flows is achieving adequate grid resolution. Stable stratification created by surface cooling restricts the size of turbulent eddies, resulting in smaller turbulent length scales (relative to those in a convective boundary layer, for example) to resolve in an LES model. The numerical modeling of downslope flows is further complicated for real case studies in the presence of complex terrain, where in addition to resolving highly-variable topography, nonuniform surface effects such as topographic shading, slope effects on radiation, and soil and land use characteristics must be considered.

In this work, the evening transition to downslope flows on a mountain slope with complex terrain is examined using high-resolution simulations. The Weather Research and Forecasting (WRF) model is employed with an immersed boundary method (IBM) that was implemented by Lundquist *et al.* (2010, 2012). The IBM gridding technique removes the restrictions on terrain slope that are associated with WRF's traditional terrain-following vertical coordinate (e.g., Janjic, 1977; Mahrer, 1984; Klemp *et al.*, 2003). The coupling of WRF's radiation, land surface, and surface layer models to IBM is documented in Lundquist *et al.* (2010). The chosen case study is focused on the eastern slope of Granite Mountain, Utah, which was heavily instrumented during the Mountain Terrain Atmospheric Modeling and Observations (MATERHORN) project (Fernando *et al.*, 2015). The model is used to explore the spatial and temporal development of downslope flow along this portion of Granite mountain, and several comparisons to MATERHORN field data are made.

2 Observations of downslope flows on Granite Mountain

Observations of downslope flows on Granite Mountain during the MATERHORN field campaign were focused on a region of the east slope, particularly at 5 meteorological towers referred to as ES1-5 (figure 1). Continuous observations were made in both fall 2012 and spring 2013, including several intensive observation periods (IOPs) in both seasons. A thorough review of the structure and turbulence characteristics of the downslope flows at ES2-5 during the fall 2012 field campaign is provided by Grachev *et al.* (2015). In setting up the field experiment, it was expected that the propagation of the shadow front along the east slope at sunset would control the development of downslope flows (Fernando *et al.*, 2015), as observed in the studies of Nadeau *et al.* (2013) and Katurji *et al.* (2013). The evening transition was found to be correlated to shadow front propagation during one spring IOP (spring IOP 4, Lehner *et al.*, 2015). However, during the fall, the evening transition was found to be uncorrelated to the passage of the shadow front (Fernando *et al.*, 2015), with both cooling slab and front formation transitions observed. It was hypothesized by Lehner *et al.* (2015) that seasonal differences in shadow propagation could influence the evening transition on the east slope.

In this work, modeling efforts are focused on two MATERHORN IOPs: fall IOP 6 (October 14-15, 2012) and spring IOP 4 (May 11-12, 2013). Both of these IOPs were classified as "quiescent," meaning that the 700-hPa wind speed was less than 5 m/s and that downslope flows could develop with minimal influence from regional scale effects. In section 4, shadow propagation and downslope flow development are first discussed based on results for fall IOP 6. Then, a seasonal comparison is made with results from spring IOP 4. Finally, several field comparisons are made based on the availability of field data during each IOP.

3 Model configuration

The study site of Granite Mountain, Utah is modeled using a nested ideal WRF setup. The inner domain covers the topography of interest, as shown in figure 1. It is a 15×15 km grid with $N_x \times N_y = 300 \times 300$ points, resulting in a horizontal grid spacing of $\Delta x = \Delta y = 50$ m. It should be noted that modeling flow on Granite Mountain at this resolution in standard WRF (without IBM) is not infeasible due to the errors associated with terrain-following coordinates in regions of steep terrain (e.g., Janjic, 1977; Mahrer, 1984; Klemp *et al.*, 2003). On the present 50 m grid, the maximum local slope is roughly 55 degrees. The outer domain has flat terrain at an elevation of 1300 m ASL and is 45×45 km with $\Delta x = \Delta y = 150$ m (a grid nest ratio of 3) and periodic horizontal boundary conditions. Both the inner and outer domains are 4 km in height with $N_z = 100$ grid points. Exponential grid stretching is employed such that the vertical grid spacing $\Delta z \approx 10$ m near the ground and $\Delta z \approx 70$ m near the top of the domain. The bottom boundary condition for each velocity component is no-slip: $U_s = (u_s, v_s, w_s) = (0, 0, 0)$ m/s, where s denotes the immersed boundary surface. A Neumann bottom boundary condition based on the surface sensible heat flux Q_H calculated by WRF's surface layer model (see table 1) is applied to the potential temperature θ, viz

$$\left.\frac{\partial \theta}{\partial n}\right|_s = \frac{Q_H}{\kappa_t c_p \rho}, \tag{1}$$

where n is normal to the immersed boundary surface, κ_t is the eddy diffusivity for temperature, c_p is the specific heat capacity of air at constant pressure, and ρ is the air density. In equation (1), both κ_t and ρ are evaluated at ghost points below the immersed boundary as defined in Lundquist *et al.* (2010, 2012). Rayleigh damping is employed within the top 500 m of both domains. The time step is $\Delta t = 0.27$ s on the inner domain and $\Delta t = 0.8$ s on the outer domain. For the inner domain, the topography of Granite Mountain is read from 1/3 arc-second (approximately 10 m) data from the United States Geological Survey (USGS) National Elevation Dataset. Realistic land-use (figure 2a) and soil-type (figure 2b) data are also included. Land-use data is read from a 1 arc-second (approximately 30 m) resolution dataset and soil-type data is read from a 30 arc-second (approximately 1 km) resolution dataset, both created for 4DWX, an operational model used at Dugway Proving Ground, where Granite Mountain is located (Liu *et al.*, 2008). For the outer domain, a constant land-use of "shrubland" and a constant soil-type of "silt loam" are used. Note that the outer domain is essentially treated as a buffer between the topography of interest and the computational boundary, thus the results from that domain are not examined.

The model is initialized in typical ideal WRF fashion using a single input sounding that is applied to every x-y point in both domains. The input sounding contains potential temperature θ, vapor mixing ratio q_v, and horizontal velocity (u,v) as a function of height. The potential temperature and vapor mixing ratio fields are initialized from radiosonde data collected during the chosen MATERHORN IOPs (figure 3). The vapor mixing ratio is calculated using dewpoint temperature and pressure data from the radiosonde. The radiosonde launch site was approximately 15 km west of Granite Mountain (the "Playa" site in Fernando *et al.*, 2015, see figure 3 therein). The potential temperature profiles at Playa are quite similar to those from another site approximately 15 km east of Granite Mountain (referred to as "Sagebrush" in Fernando *et al.*, 2015), especially above the surface layer (not shown). This indicates that the Playa potential temperature profiles are likely representative of the regional conditions surrounding Granite Mountain (dewpoint temperature data is not available at the Sagebrush site). Although the Playa radiosonde data includes horizontal velocity, the initial horizontal velocity is set to zero in the model such that the atmosphere is quiescent before thermally-driven flows develop. To allow for adequate model spin-up before sunset, the fall simulation is initialized at 10:10 MST based on radiosonde data from 10:08 MST. The spring simulation is initialized at 13:20 MST based on radiosonde data from 13:18 MST. Both the inner and outer domains are initialized at the same time.

The primary forcing in the model is incoming solar radiation, moderated by slope and topographic shading effects. The WRF-specific radiation, land-surface, and surface layer schemes used are shown in table 1. The model soil moisture is initialized as 0.10 in the fall case and 0.15 in the spring case based on the average seasonal values presented by Jensen *et al.* (2015). Although Lundquist *et al.* (2012) enabled the Smagorinsky turbulence model in WRF-IBM, it is not yet coupled with the land surface model or surface layer scheme. A constant eddy viscosity $\nu_t = 0.5$ m^2/s is therefore used on the inner nest. This value of ν_t was found to be the smallest possible value needed to maintain stability of the model. Due to increased radiative forcing in the spring case, $\nu_t = 1.0$ m^2/s is necessary for stability during model spin-up. However, ν_t is reduced to 0.5 m^2/s at 18:15 MST as downslope flows develop. A larger eddy viscosity value of $\nu_t = 10$ m^2/s is used on the outer nest. The eddy diffusivity is $\kappa_t = \nu_t / Pr_t$, where the turbulent Prandtl number $Pr_t = 1/3$, the default condition in WRF.

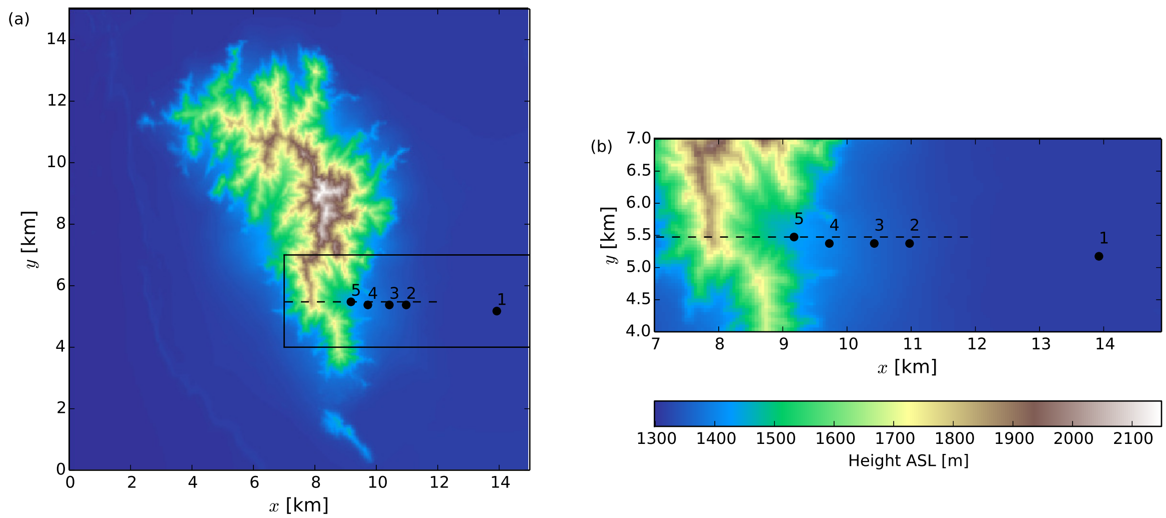

Figure 1: (a) The topography of Granite Mountain, as represented in the inner nest of the WRF-IBM domain. (b) A zoomed-in view of the east slope study area. The locations of east slope towers ES1-5 are shown in both plots (black dots), as is the horizontal cross section shown in figure 6 (dashed line).

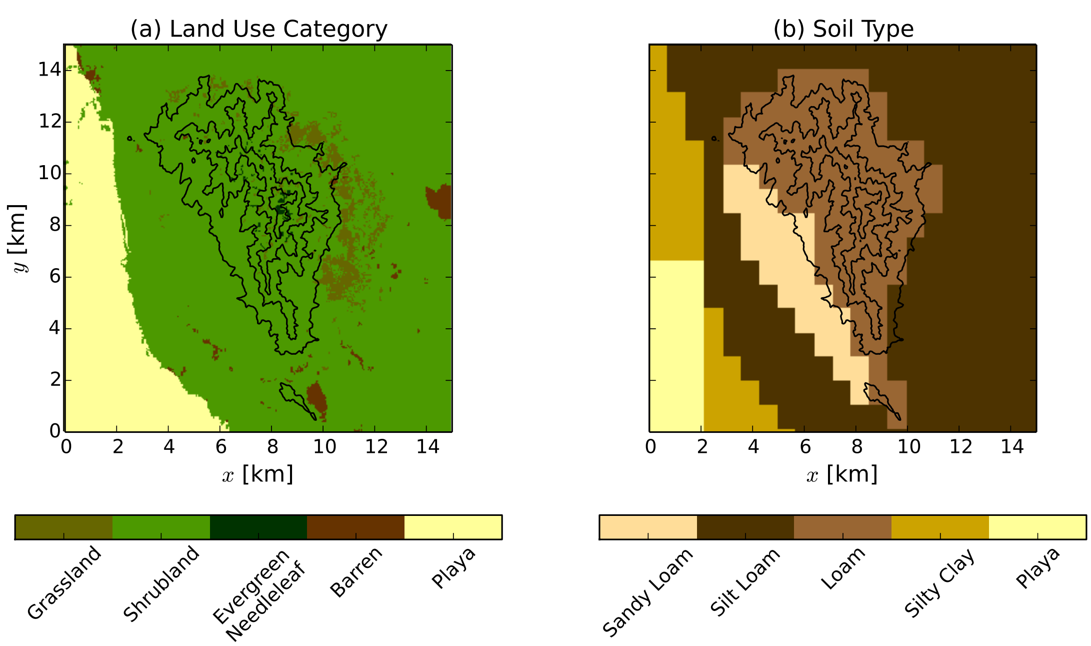

Figure 2: The (a) land-use and (b) soil-type data included in the inner nest of the WRF-IBM domain. The topography of Granite Mountain is shown by black contour lines between $z = 1400$ and $z = 2000$ m ASL with an interval of 200 m.

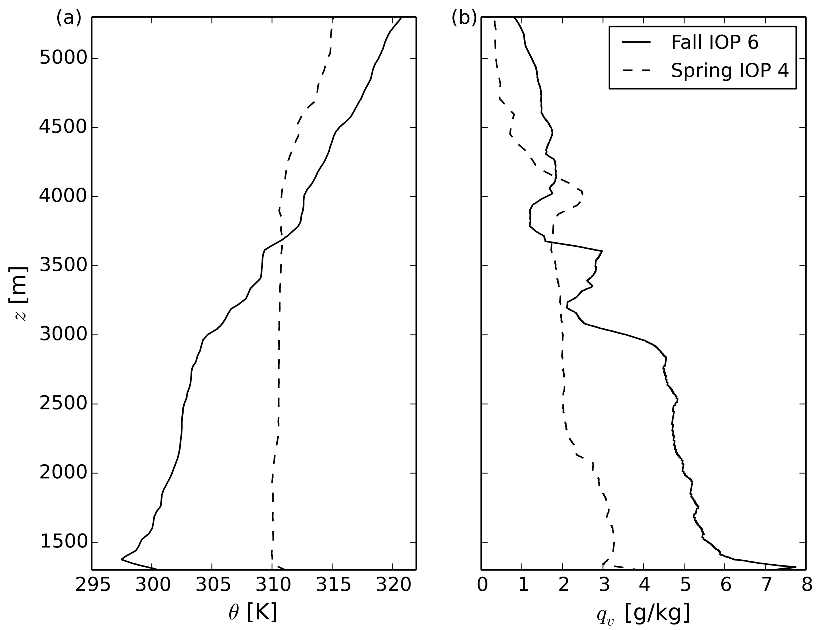

Figure 3: (a) Potential temperature θ (b) vapor mixing ratio q_v from radiosondes launched at Playa site near Granite Mountain during fall IOP 6 and spring IOP 4.

Module	Scheme	WRF namelist variable	Value
Shortwave radiation	Dudhia scheme	`ra_sw_physics`	1
Longwave radiation	RRTM scheme	`ra_lw_physics`	1
Land surface	Noah	`sf_surface_physics`	2
Surface layer	MM5 similarity	`sf_sfclay_physics`	91

Table 1: Summary of WRF modules.

4 Results

4.1 Downslope flow development

Downslope flows generally develop after a change in the surface sensible heat flux Q_H from positive during the day to negative at night. Model results suggest that on the east slope of Granite Mountain, this change in Q_H is driven by topographic shading (figure 4). In WRF, topographic shading is calculated based on the position of the sun relative to the model topography. A given location (grid point) is deemed to be "shaded" if some topography exists between it and the sun. In other words, a location that is shaded has experienced "local sunset." As the sun sets to the west of Granite Mountain during the fall, the upper elevations of the east slope become shaded first, and Q_H becomes negative in these regions (figure 4a-b). The shadow front then propagates to the northeast, moving down the east slope with a corresponding reversal of Q_H (figure 4c-f). At later times when the east slope is fully shaded (figure 4e-f), the west slope still experiences incoming solar radiation Q_{Si} and Q_H remains positive. Thus, downslope flows develop later on the west slope than on the east slope.

The modeled downslope flow development on the east slope is driven by the reversal of the surface sensible heat flux after local sunset. Potentially cool air forms first at higher elevations (upslope of ES5) where the shadow is present. It then begins to flow downslope toward ES5 (figure 5a). The topography of the drainage basin in which the east slope towers are situated dictates the direction of the downslope flow. Because the shadow propagates from southwest to northeast, the northeast-facing slopes upslope of ES5 are shaded first. Therefore the downslope flow develops there and flows predominantly from the southwest (figure 5a-b). The south- and southwest-facing slopes upslope of ES5, on the other hand, experience positive Q_{Si} for a longer time. Thus some upslope flow remains in these regions (see red regions in figure 5), even as the downslope flow develops elsewhere. Although the presence of the shadow initiates the downslope flow at higher elevations, the downslope flow reaches lower elevations of the mountain (ES5 and below) before local sunset (figure 5b-d). The downslope flow at ES5 and downslope of it is predominantly westerly, following the relatively uniform topography there.

Despite the three-dimensionality of the flow on the east slope, an east-west slice of the domain can provide insight into the flow development, especially at lower elevations. The developing downslope flow forms a stagnation front that moves gradually downslope, passing each ES tower in succession (figure 6). As explained by Hunt *et al.* (2003), the stagnation front is the boundary between the developing downslope flow and the remaining convective upslope flow, and is visible in each panel of figure 6. Physically, it can be thought of as the "nose" of the downslope flow.

The development of the downslope flow can also be visualized using a virtual distributed temperature sensor (DTS). In the field, DTS systems measure near-ground temperature along an optical sensor cable over long distances, and have been used to examine downslope flow development (Fernando *et al.*, 2015). Virtual DTS output can be extracted from model results by interpolating near-ground temperature data along a line, as shown in figure 7a between ES5 and ES2. A sharp drop in temperature progresses downslope along the virtual DTS following the stagnation front (see black dots in figure 7a and vertical lines in figure 7b-e). The modeled 30 m wind direction at the ES tower locations becomes consistently downslope ($\approx 270^o$) after the stagnation front passes (figure 7b-e). As seen previously in figures 5 and 6, the downslope flow reaches successive ES towers before local sunset (see dashed lines in figure 7a,b-e) and thus before the local surface sensible heat flux reverses. Although the average speed of the stagnation front between ES5 and ES2 (roughly 2.0 km/hr) is less than the average speed of the shadow front (roughly 3.1 km/hr), the downslope flow still reaches the ES towers before the shadow. A comparison of the virtual DTS output to DTS data from the MATERHORN field program is presented in section 4.3.2.

4.2 Seasonal comparison

It was hypothesized by Lehner *et al.* (2015) that seasonal differences in shadow propagation on Granite Mountain could affect downslope flow development. Therefore, results from a spring IOP 4 simulation are presented for comparison to those from fall IOP 6. During the spring, the shadow propagates from northwest to southeast (figure 8). This is in contrast to the fall, when the shadow propagates from southwest to northeast (figure 4). In both seasons, however, the shadow position controls the sign of the surface sensible heat flux. Q_H is predominantly negative on eastward-facing slopes as the sun sets, while Q_H remains positive on westward-facing slopes until later in the day.

In the spring, as in the fall, potentially cool air forms first at higher elevations upslope of ES5 where the shadow is present. This cool air then drains downslope toward ES5 (figure 9a). However, there is a noticeable difference in the direction of downslope flow development on the east slope between the fall and spring cases. Because the shadow moves from northwest to southeast in the spring, the drainage basin above ES5 is shaded relatively uniformly, causing downslope flow to develop from the west-northwest (figure 9b). Conversely in the

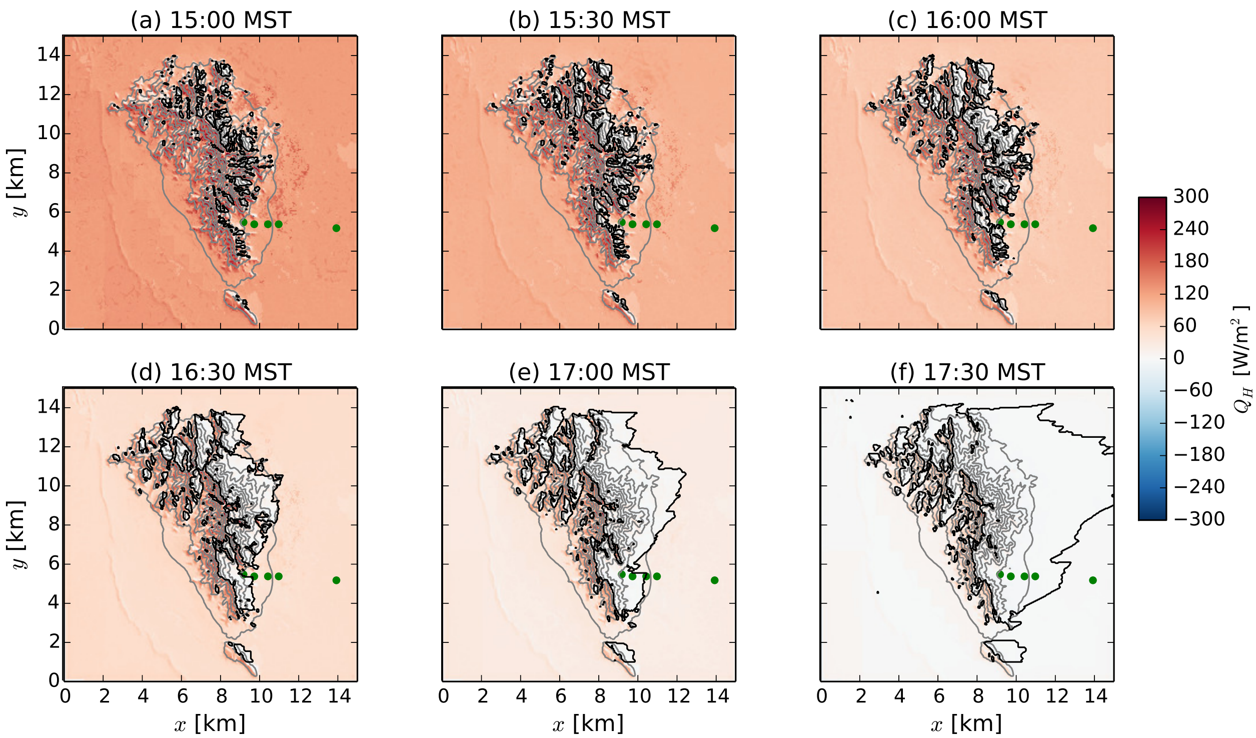

Figure 4: Modeled shadow propagation (black contours) and surface sensible heat flux Q_H (color scale) on the east slope of Granite Mountain during fall IOP 6. The topography of Granite Mountain is shown by gray contour lines between $z = 1350$ and $z = 2150$ m ASL with an interval of 100 m. Also shown are the locations of east slope towers ES1-5 (green dots).

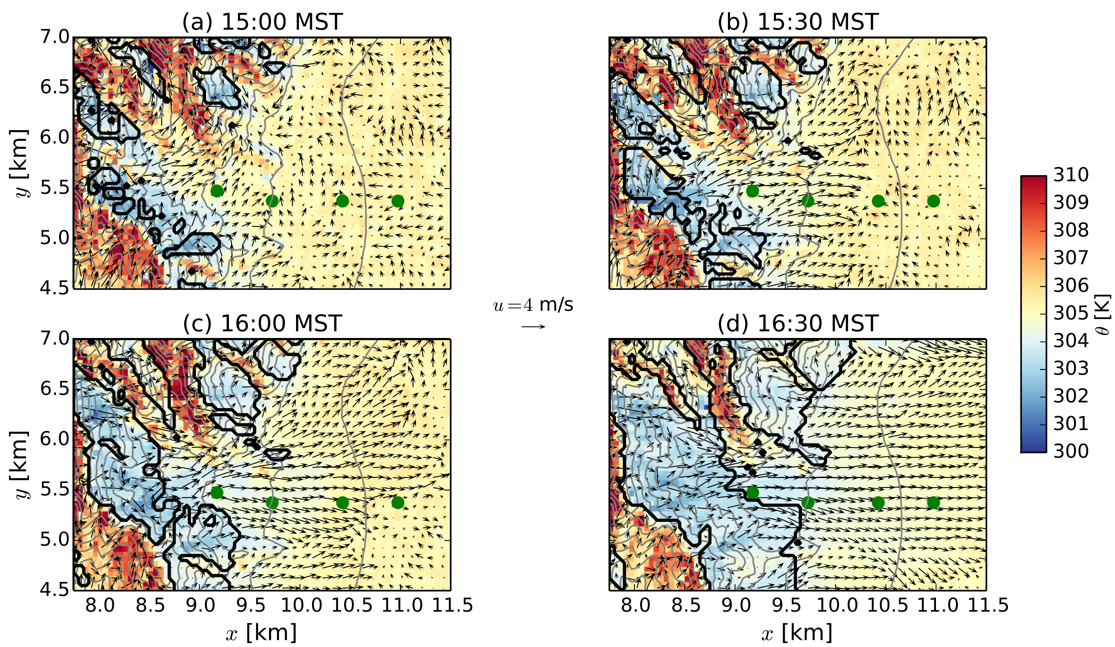

Figure 5: Zoomed-in view of the east slope of Granite Mountain during fall IOP 6. Shown are near-ground potential temperature (θ at 0.5 m AGL) and horizontal velocity vectors (u,v at 30 m AGL), as well as the shadow location (black contours). The topography of Granite Mountain is shown by gray contour lines between $z = 1350$ and $z = 2000$ m ASL with an interval of 50 m. Also shown are the locations of east slope towers ES2-5 (green dots).

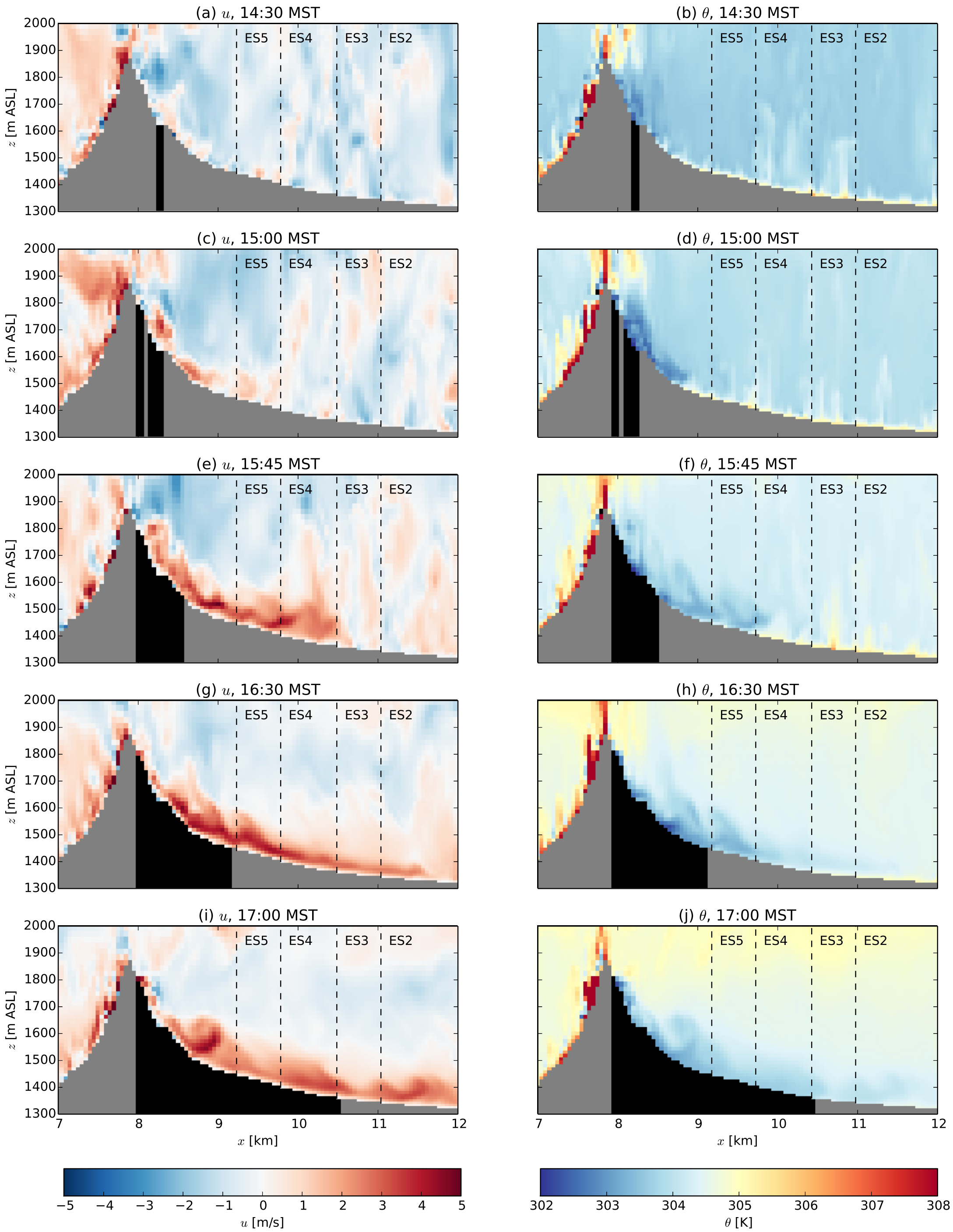

Figure 6: (a,c,e,g,i) Horizontal velocity u and (b,d,f,h,j) potential temperature θ along the horizontal cross section shown by the dashed line in figure 1. Results are shown for fall IOP 6. The black shading below the topography denotes the presence of the shadow at the given x location. Vertical dashed lines denote the approximate locations of ES towers 2-5. The time snapshots in (a)-(h) correspond to those shown in figure 5. Note that the gaps in the shadow along this cross-section are due to the two-dimensional variations in the shadow seen in figure 4, a result of the complex mountain topography.

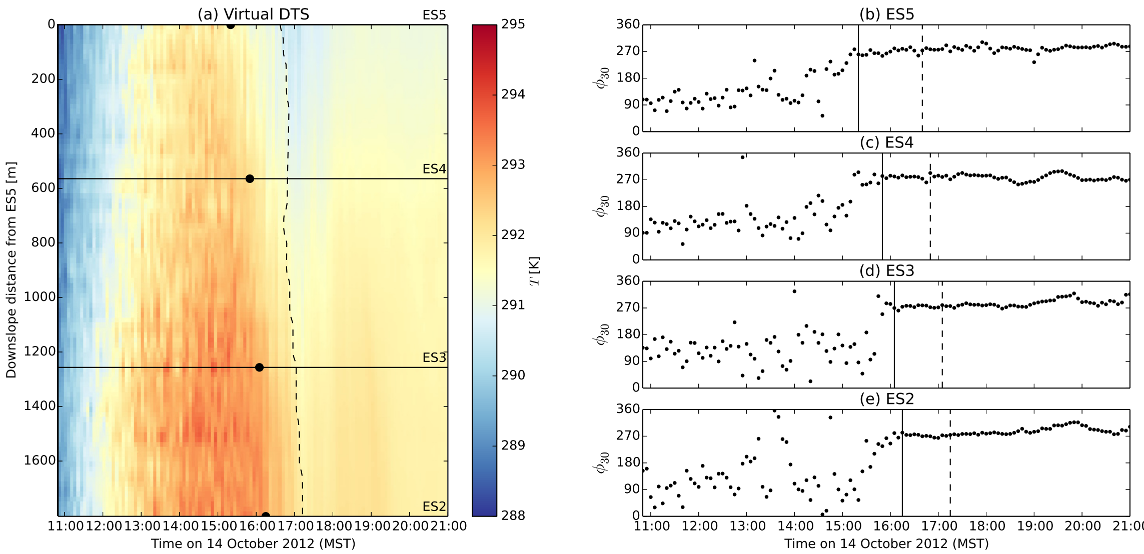

Figure 7: (a) Hovmöller diagram of virtual DTS data at 0.5 m AGL between ES5 and ES2 for fall IOP 6. (b)-(e) The modeled 30 m wind direction ϕ_{30} at ES5-2. Horizontal lines in (a) denote the locations of ES towers along the length of the virtual DTS (ES5 is the top boundary and ES2 is the lower boundary). Black dots in (a) denote the approximate time of downslope flow development at ES5-2, also denoted by vertical lines in (b)-(e). Visualizations of the flow at these times can be found in figures 5 and 6. The passage of the shadow at each ES tower is also denoted by a dashed line in (a)-(e).

fall, since the shadow moves from southwest to northeast, the northeast-facing slopes above ES5 are shaded initially and the downslope flow develops from the west-southwest (figure 5a-b). The flow downslope of ES5 is ultimately affected by the development upslope. In the spring, the flow downslope of ES5 maintains a strong northwesterly component (figure 9c-d), while in the fall, the flow below ES5 is predominantly westerly (figure 5c-d).

There are also seasonal differences in the speed and timing of the downslope flow development between ES5 and ES2, as seen when comparing virtual DTS output for the spring case (figure 10) to that from the fall case (figure 7). Most notably, the stagnation front closely follows the shadow front down the slope in the spring (see figures 9 and 10); both fronts have a similar propagation speed of roughly 3.1 km/hr. Conversely in the fall, the stagnation front arrived at successive ES towers before the shadow front (see figures 5 and 7). A similar correlation between shadow propagation and downslope flow transition was found by Lehner *et al.* (2015) in their analysis of field data from MATERHORN spring IOP 4. During the fall MATERHORN IOPs, however, the positions of the stagnation front and the shadow front were generally uncorrelated (Fernando *et al.*, 2015). This seasonal difference is likely due to the close alignment of the major axis of the drainage basin and the shadow propagation direction in the spring. Additionally, the increased spring soil moisture likely delays the downslope flow transition such that it follows the shadow front.

4.3 Comparison to field data

4.3.1 *Surface energy budget data*

The surface sensible heat flux is dependent on the surface energy budget, viz (Zardi & Whiteman, 2013)

$$Q_H = -(R_n + Q_G + Q_L), \tag{2}$$

$$R_n = Q_{Si} + Q_{Li} - Q_{So} - Q_{Lo}. \tag{3}$$

where R_n is the net radiation, Q_G is the ground heat flux, Q_L is the latent heat flux, Q_{Si} is the incoming shortwave radiation, Q_{Li} is the incoming longwave radiation, Q_{So} is the outgoing shortwave radiation, and Q_{Lo} is the outgoing longwave radiation. Based on a comparison with field observations at ES5, the model generally captures the surface energy balance accurately (figure 11). Note that field data is only shown when available and that the variability in the spring IOP 4 data is likely due to the presence of clouds, which are not captured in the model.

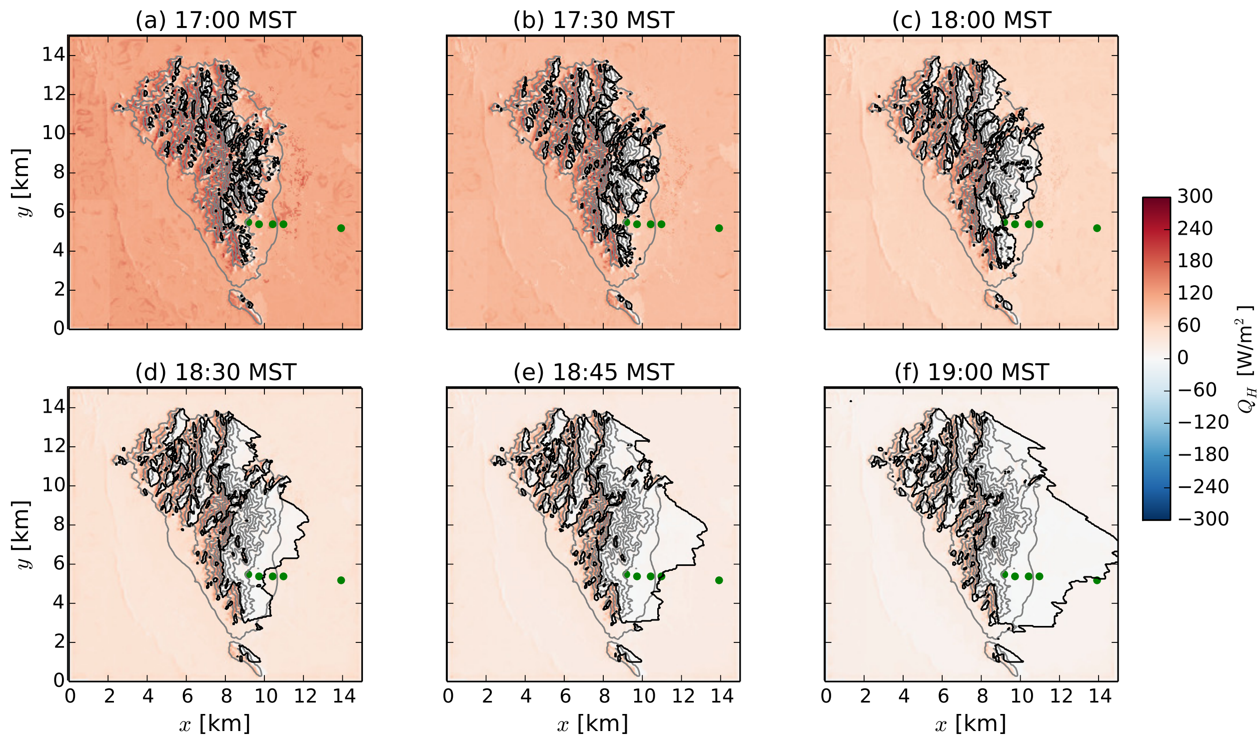

Figure 8: Modeled shadow propagation (black contours) and surface sensible heat flux Q_H (color scale) on the east slope of Granite Mountain during spring IOP 4. The topography of Granite Mountain is shown by gray contour lines between $z = 1350$ and $z = 2150$ m ASL with an interval of 100 m. Also shown are the locations of east slope towers ES1-5 (green dots).

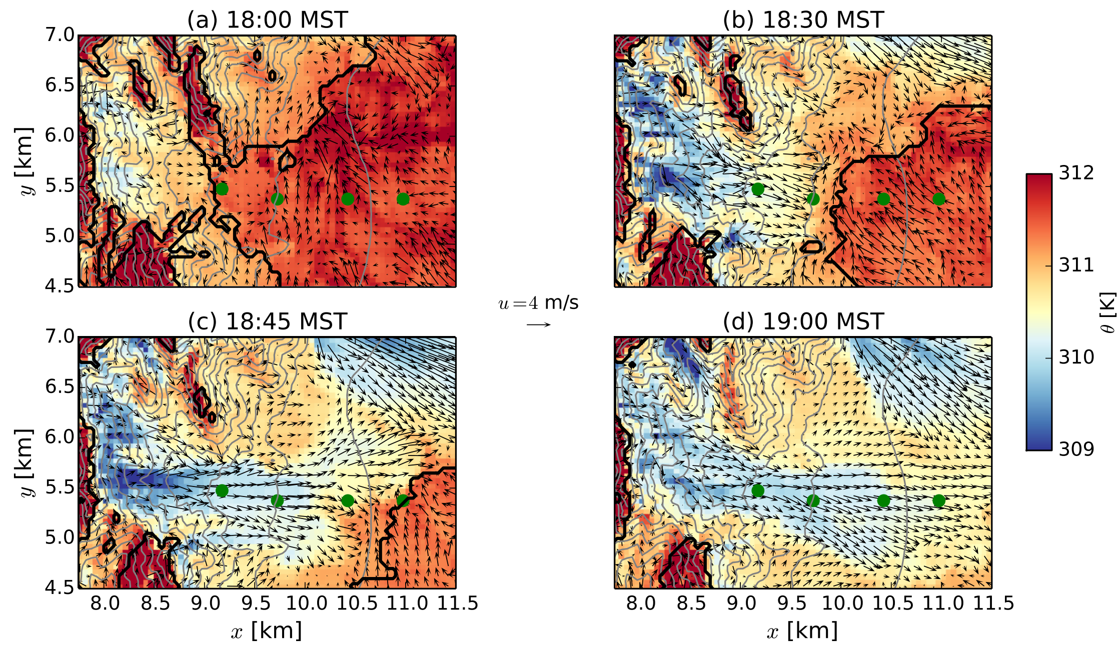

Figure 9: Zoomed-in view of the east slope of Granite Mountain during spring IOP 4. Shown are near-ground potential temperature (θ at 0.5 m AGL) and horizontal velocity vectors (u,v at 30 m AGL), as well as the shadow location (black contours). The topography of Granite Mountain is shown by gray contour lines between $z = 1350$ and $z = 2000$ m ASL with an interval of 50 m. Also shown are the locations of east slope towers ES2-5 (green dots).

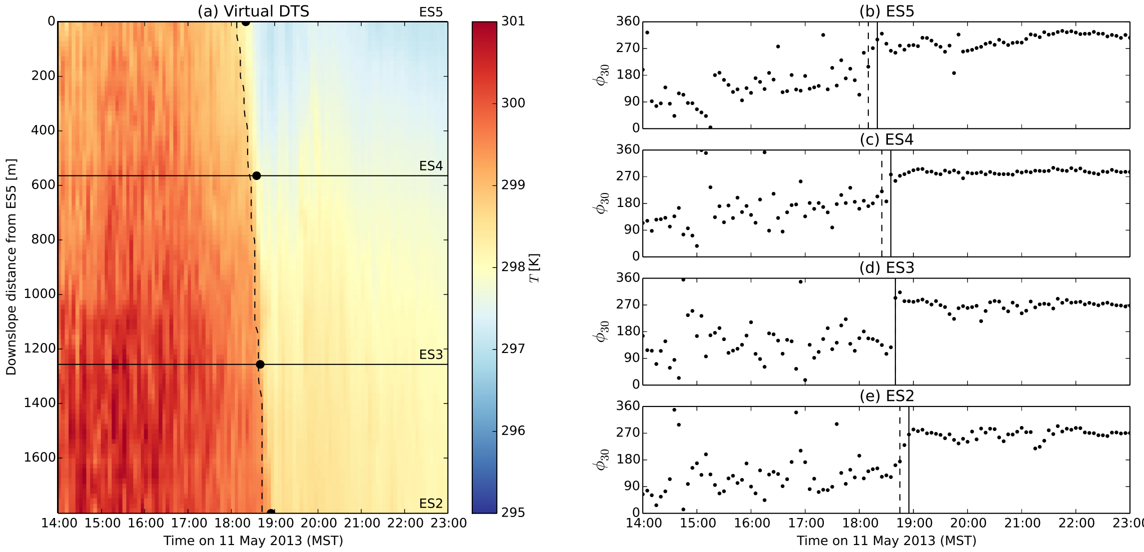

Figure 10: (a) Hovmöller diagram of virtual DTS data at 0.5 m AGL between ES5 and ES2 for spring IOP 4. (b)-(e) The modeled 30 m wind direction ϕ_{30} at ES5-2. Horizontal lines in (a) denote the locations of ES towers along the length of the virtual DTS (ES5 is the top boundary and ES2 is the lower boundary). Black dots in (a) denote the approximate time of downslope flow development at ES5-2, also denoted by vertical lines in (b)-(e). The passage of the shadow at each ES tower is also denoted by a dashed line in (a)-(e).

Starting at midday in both cases, the modeled Q_{Si} decreases gradually until a sharp drop at local sunset (denoted by the vertical dotted lines in figure 11), when ES5 becomes shaded. The remaining Q_{Si} after this time is due to diffuse shortwave radiation, after which Q_{Si} goes to zero. The modeled net radiation R_n follows the trend of Q_{Si}, although its magnitude is modulated by the other radiation components. Since Q_L is small, the surface sensible heat flux Q_H, which drives thermally-driven flows in the model, is controlled by R_n and Q_G. Focusing on the spring IOP 4 case (figure 11d), when more field data is available for comparison, the modeled Q_H shows several differences from the observed value. Most notably, the available energy at the surface in the model is incorrectly partitioned between Q_H and Q_G, causing the modeled Q_H to be smaller and the modeled Q_G to be larger than the observed values after local sunset. Additionally, the modeled Q_H becomes negative 1-2 hours after local sunset, while the observations show a more immediate change. Based on the general agreement between the modeled and observed R_n, these differences are likely a consequence of the land surface model or soil initialization parameters.

4.3.2 Distributed temperature sensor data

Field DTS data were collected during the fall 2012 MATERHORN field campaign (Fernando *et al.*, 2015, DTS data were not collected during spring 2013) to capture the near-ground temperature signal of downslope flows on the east slope. The DTS cable was mounted at 0.5 m AGL between ES2 and ES5. Observed DTS data from fall IOP 6 is therefore included in figure 12 for comparison to the model results in figure 7. The field and model results are qualitatively similar, showing a successive transition to sustained downslope flow at ES5-2 corresponding to a drop in near-surface temperature. There are, however, several differences to note. First, the near-surface temperature range is larger in the field than in the model. Daytime (nighttime) cold (warm) temperature biases have been observed previously in WRF (Massey *et al.*, 2014). The semi-idealized model, however, is not expected to capture the full range of temperature variability seen in the field. Second, the observed wind direction is reported for 10 m AGL, while the modeled wind direction is reported for 30 m AGL. This is because the downslope jet height is typically below 10 m AGL in the observations, while it is approximately 30 m AGL in the model. For further discussion of the jet height, see section 4.3.3.

Additionally, the downslope flow front progresses

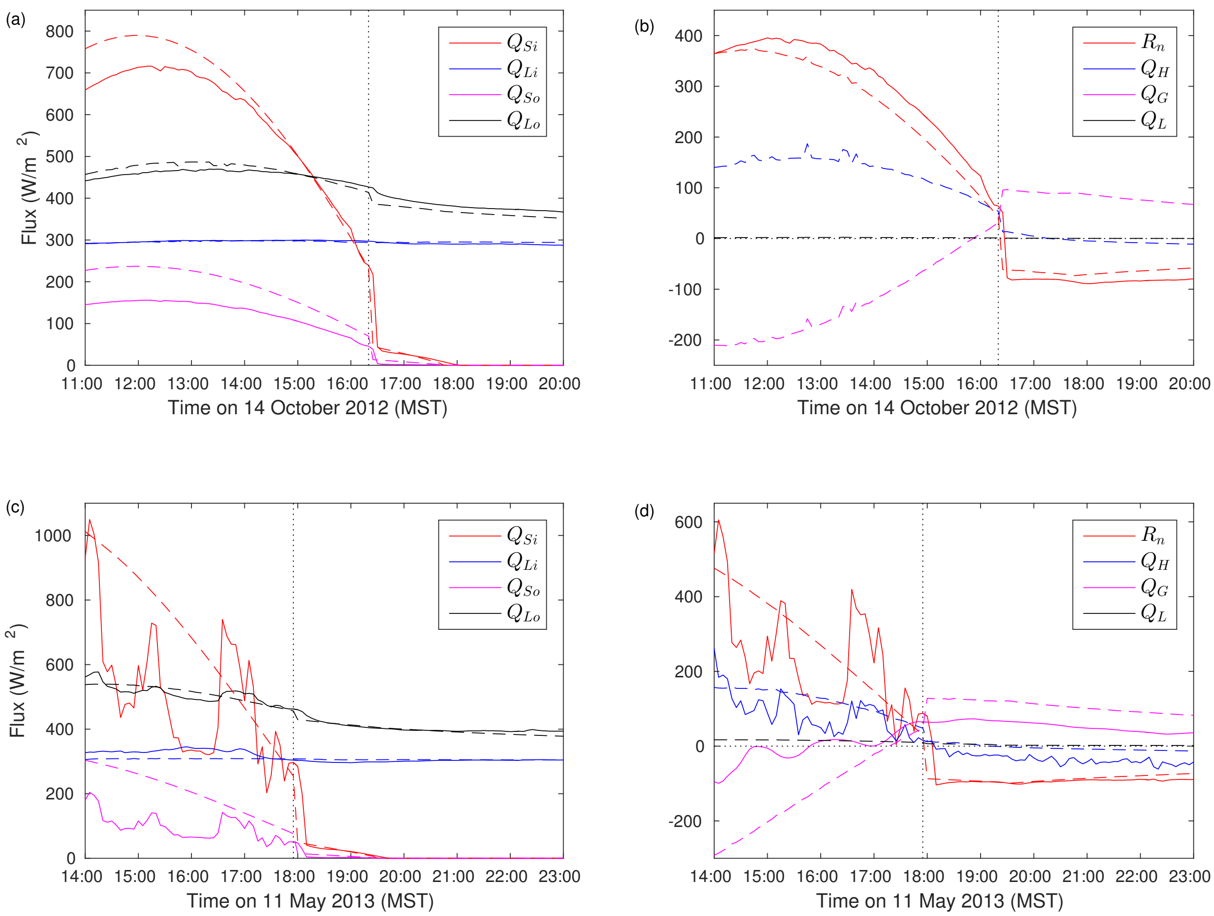

Figure 11: Modeled (−−) and observed (—) surface energy budget quantities at ES5 during (a,b) fall IOP 6 and (c,d) spring IOP 4. Observed data are included when available. The vertical dotted line indicates local sunset in the model.

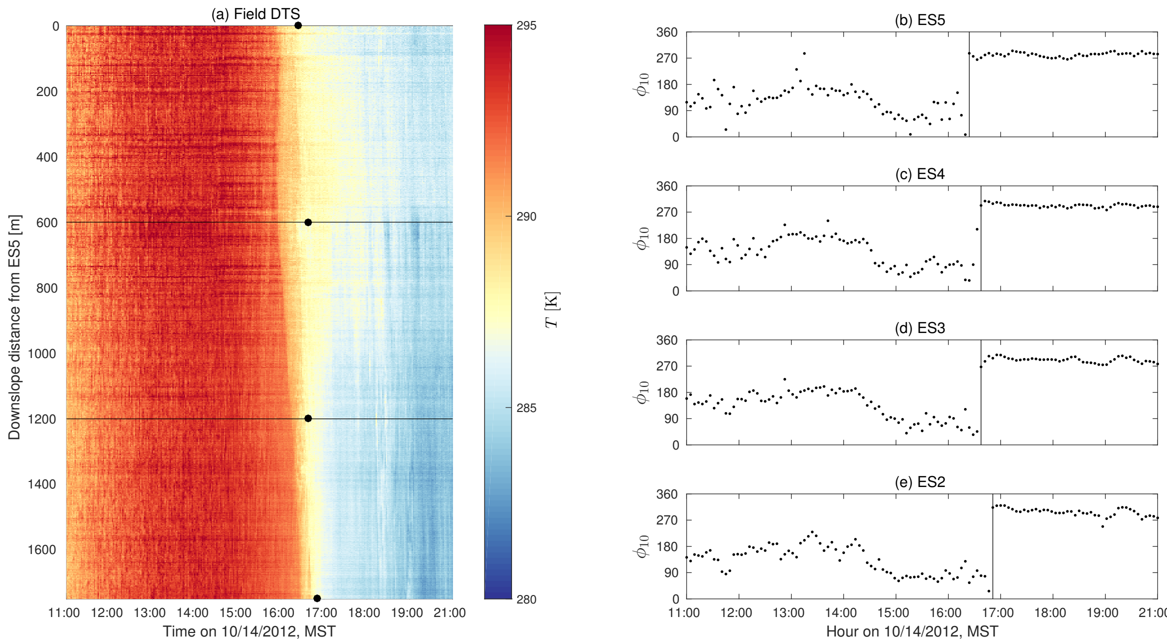

Figure 12: (a) Hovmöller diagram of field DTS data (Fernando *et al.*, 2015) at 0.5 m AGL between ES5 and ES2 for fall IOP 6. (b)-(e) The observed 10 m wind direction ϕ_{10} at ES5-2. Horizontal lines in (a) denote the locations of ES towers along the length of the virtual DTS (ES5 is the top boundary and ES2 is the lower boundary). Black dots in (a) denote the approximate time of downslope flow development at ES5-2, also denoted by vertical lines in (b)-(e).

downslope faster in the observations than in the model. While the observed front moves from ES5 to ES2 with a speed of roughly 3.6 km/hr, the modeled front has a speed of roughly 2.0 km/hr. Several factors could contribute to this difference, including the strength of the daytime convective flow, the modeled surface characteristics (soil moisture, land use, soil type), or the simple turbulence closure used in the model.

4.3.3 Tethersonde data

While the MATERHORN ES towers were limited to measurements within 20-30 m AGL, tethersonde measurements collected during spring IOP 4 near ES3 reached approximately 200 m AGL (Lehner *et al.*, 2015). The tethersonde data includes velocity, temperature, and pressure, and provides a relatively high-resolution picture of near-ground conditions. Comparison of tethersonde profiles to model results at the same location during spring IOP 4 (figure 13a,c) highlights the primary deficiency of the current model setup. That is, the height of the near-ground downslope velocity maximum, often referred to as the "jet height," is too high in the model (roughly 30 m AGL) as compared to the observations (roughly 5-10 m AGL). The observations show a highly stable flow layer and a near-surface potential temperature deficit of roughly 6 K. The strong stability prevents momentum from mixing vertically, keeping the jet height low. In the model, a near-ground potential temperature deficit of less than 1 K occurs, allowing the vertical exchange of momentum and an increase in the jet height. This leads to a slight reduction in the maximum jet velocity, which is roughly 2-3 m/s in the model but can be up to nearly 4 m/s in the observations (see figure 13). The difference between the modeled and observed near-ground potential temperature deficit is likely a consequence of the reduced Q_H in the model, as discussed in section 4.3.1.

5 Conclusions

In this study, the WRF-IBM model was used to explore the development of downslope flows on the east slope of Granite Mountain, Utah. The immersed boundary method allowed WRF to represent the complex topography of Granite Mountain accurately at high resolution, which would not have been possible with the limitations of WRF's traditional terrain-following vertical coordinate. Realistic initialization and forcing were used in the model, including high-resolution land-use and soil-type data, as well as radiosonde data from several MATERHORN IOPs.

Downslope flows were found to develop on the east

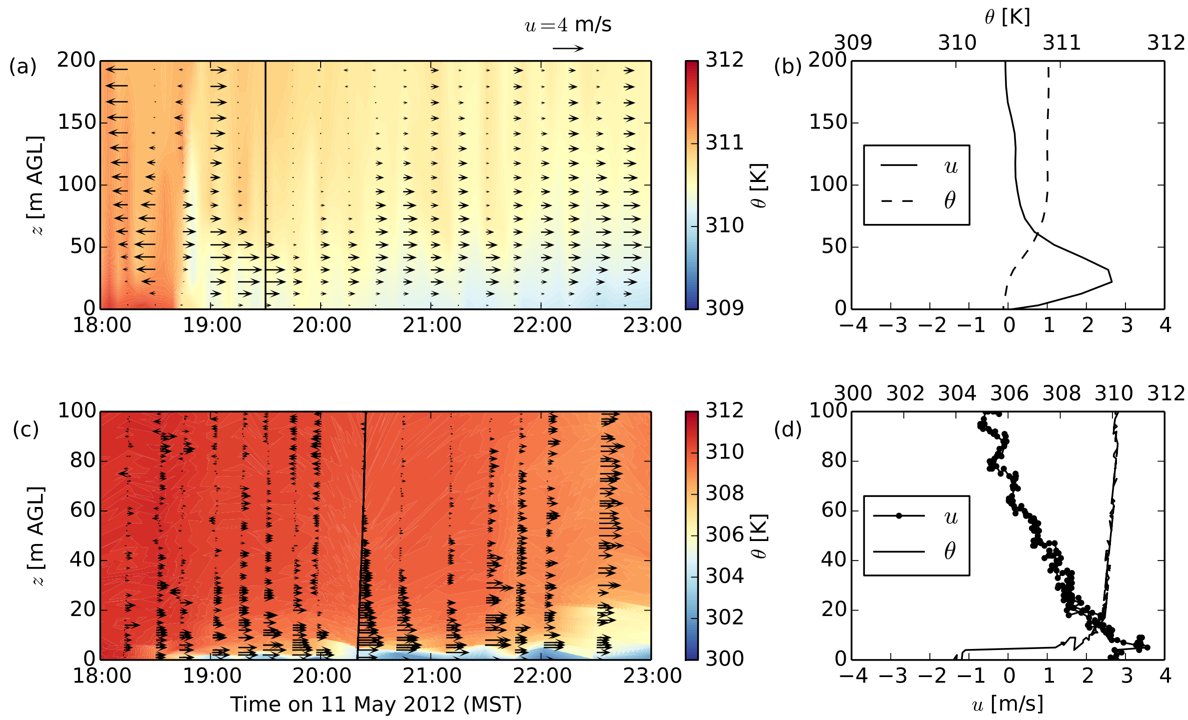

Figure 13: (a) Modeled and (c) field potential temperature θ and horizontal velocity u over time at the east slope tethersonde site during spring IOP 4. Representative (b) model and (d) field θ and u profiles at the times indicated by the vertical lines in (a) and (c), respectively. Note the difference in vertical axis extent between plots (a-b) and (c-d).

slope of Granite Mountain after sunset, when topographic shading led to a negative net radiation and a negative surface sensible heat flux in shaded areas. The upper elevations of the east slope were shaded first, and the cool air that developed there flowed downslope, forming a stagnation front between the developing downslope flow and unshaded convective (generally upslope) regions. While the modeled downslope flow development was similar in fall and spring cases, the seasonal differences in shadow propagation and soil moisture were shown to affect the predominant downslope flow direction, as well as the speed and timing of downslope flow development on the east slope.

The downslope flow development in the model is qualitatively consistent with the the MATERHORN field observations (Lehner *et al.*, 2015; Fernando *et al.*, 2015). In the spring case, both the modeled and observed results show that downslope flow development follows the shadow front, while in the fall, the timing of flow development is less correlated to the passage of the shadow front. The strong influence of topographic shading on the surface energy balance in the model suggests that a downslope flow transition mechanism other than the cooling slab (Fernando *et al.*, 2013) or front formation (Hunt *et al.*, 2003) mechanisms, both of which assume spatially uniform surface cooling, may be present in regions of complex terrain. Although these transition types were observed on Granite Mountain during the fall (Fernando *et al.*, 2015), they were not seen in the fall model results. A larger suite of both fall and spring cases would be necessary to fully examine the applicability of these analytical models on Granite Mountain, or in other locations with complex terrain.

Comparison to tethersonde measurements on the east slope during the spring (Lehner *et al.*, 2015) highlights the primary deficiency of the current model setup. Although downslope flow develops in the model, the near-surface temperature deficit is smaller than that observed in the field. This allows the modeled jet to grow vertically, increasing the jet height and reducing the maximum downslope velocity relative to field observations. Improvements in the modeled near-surface temperature deficit could be made using the suggestions of Massey *et al.* (2014), or with additional modifications to the soil initialization, land surface model, or surface layer scheme. Improving the agreement between the modeled and field velocity profiles would also likely require the use of a more sophisticated turbulence closure scheme (such as Smagorinsky or TKE 1.5 in WRF), as well as increased resolution near the ground, which is the subject of future work.

6 Acknowledgements

The simulations used in this work were performed on the University of California, Berkeley Savio cluster. This work was funded by the Office of Naval Research Award #N00014-11-1-0709, Mountain Terrain Atmospheric Modeling and Observations (MATERHORN) Program. We acknowledge the entire MATERHORN field team, as well as the staff of Dugway Proving Ground, for their efforts in collecting field data. We are especially grateful to M. Lehner for sharing tethersonde data, to C. W. Higgins for sharing DTS data, and to D. Jensen for sharing ES tower data with us. We also acknowledge A. D. Anderson-Connolly and D. J. Wiersema for their help in setting up the model.

References

Axelsen, S. L., & van Dop, H. 2009. Large-eddy simulation of katabatic winds. Part 2: Sensitivity study and comparison with analytical models. *Acta Geophys.*, **57**(4), 837–856.

Fernando, H. J. S., Verhoef, B., Di Sabatino, S., Leo, L. S., & Park, S. 2013. The Phoenix evening transition flow experiment (TRANSFLEX). *Boundary-layer Meteorol.*, **147**(3), 443–468.

Fernando, H. J. S., Pardyjak, E. R., Di Sabatino, S., Chow, F. K., De Wekker, S. F. J., Hoch, S. W., Hacker, J., Pace, J. C., Pratt, T., Pu, Z., *et al.* 2015. The MATERHORN: Unraveling the Intricacies of Mountain Weather. *B. Am. Meteorol. Soc.*, **96**(11), 1945–1967.

Grachev, A. A., Leo, L. S., Di Sabatino, S., Fernando, H. J. S., Pardyjak, E. R., & Fairall, C. W. 2015. Structure of turbulence in katabatic flows below and above the wind-speed maximum. *Boundary-layer Meteorol.*, 1–26.

Grisogono, B. 2003. Post-onset behaviour of the pure katabatic flow. *Boundary-layer Meteorol.*, **107**(1), 157–175.

Grisogono, B., & Oerlemans, J. 2001. Katabatic flow: Analytic solution for gradually varying eddy diffusivities. *J. Atmos. Sci.*, **58**(21), 3349–3354.

Gutman, L. N., & Malbakhov, V. M. 1964. On the theory of katabatic winds of Antarctic. *Met. Issled.*, **9**, 150–155.

Hunt, J. C. R., Fernando, H. J. S., & Princevac, M. 2003. Unsteady thermally driven flows on gentle slopes. *J. Atmos. Sci.*, **60**(17), 2169–2182.

Janjic, Z. 1977. Pressure gradient force and advection scheme used for forecasting with steep and small scale topography. *Beitr. Phys. Atmos.*, **50**(1), 186–199.

Jensen, D. D., Nadeau, D. F., Hoch, S. W., & Pardyjak, E. R. 2015. Observations of Near-Surface Heat-Flux and Temperature Profiles Through the Early Evening Transition over Contrasting Surfaces. *Boundary-layer Meteorol.*, **159**(3), 567–587.

Katurji, M., Zawar-Reza, P., & Zhong, S. 2013. Surface layer response to topographic solar shading in Antarctica's dry valleys. *J. Geophys. Res. Atmos.*, **118**(22).

Kavčič, I., & Grisogono, B. 2007. Katabatic flow with Coriolis effect and gradually varying eddy diffusivity. *Boundary-layer Meteorol.*, **125**(2), 377–387.

Klemp, J. B., Skamarock, W. C., & Fuhrer, O. 2003. Numerical consistency of metric terms in terrain-following coordinates. *Mon. Weather Rev.*, **131**(7), 1229–1239.

Lehner, M., Whiteman, C. D., Hoch, S. W., Jensen, D. D., Pardyjak, E. R., Leo, L. S., Di Sabatino, S., & Fernando, H. J. S. 2015. A Case Study of the Nocturnal Boundary Layer Evolution on a Slope at the Foot of a Desert Mountain. *J. Appl. Meteorol. Clim.*, **54**(4), 732–751.

Liu, Y., Warner, T. T., Bowers, J. F., Carson, L. P., Chen, F., Clough, C. A., Davis, C. A., Egeland, C. H., Halvorson, S. F., Huck, T. W., *et al.* 2008. The operational mesogamma-scale analysis and forecast system of the US Army Test and Evaluation Command. Part I: Overview of the modeling system, the forecast products, and how the products are used. *J. Appl. Meteorol. Clim.*, **47**(4), 1077–1092.

Lundquist, K. A., Chow, F. K., & Lundquist, J. K. 2010. An immersed boundary method for the Weather Research and Forecasting model. *Mon. Weather Rev.*, **138**(3), 796–817.

Lundquist, K. A., Chow, F. K., & Lundquist, J. K. 2012. An immersed boundary method enabling large-eddy simulations of flow over complex terrain in the WRF Model. *Mon. Weather Rev.*, **140**(12), 3936–3955.

Mahrer, Y. 1984. An improved numerical approximation of the horizontal gradients in a terrain-following coordinate system. *Mon. Weather Rev.*, **112**(5), 918–922.

Massey, J. D., Steenburgh, W. J., Hoch, S. W., & Knievel, J. C. 2014. Sensitivity of near-surface temperature forecasts to soil properties over a sparsely vegetated dryland region. *J. Appl. Meteorol. and Clim.*, **53**(8), 1976–1995.

Nadeau, D. F., Pardyjak, E. R., Higgins, C. W., Huwald, H., & Parlange, M. B. 2013. Flow during the evening transition over steep Alpine slopes. *Q. J. Roy. Meteor. Soc.*, **139**(672), 607–624.

Prandtl, L. 1942. *Führer durch die Strömungslehre*. Vieweg und Sohn, Braunschweig.

Shapiro, A., & Fedorovich, E. 2008. Coriolis effects in homogeneous and inhomogeneous katabatic flows. *Q. J. Roy. Meteor. Soc.*, **134**(631), 353–370.

Skyllingstad, E. D. 2003. Large-eddy simulation of katabatic flows. *Boundary-layer. Meteorol.*, **106**(2), 217–243.

Smith, C. M., & Porté-Agel, F. 2014. An intercomparison of subgrid models for large-eddy simulation of katabatic flows. *Q. J. Roy. Meteor. Soc.*, **140**(681), 1294–1303.

Smith, C. M., & Skyllingstad, E. D. 2005. Numerical simulation of katabatic flow with changing slope angle. *Mon. Weather Rev.*, **133**(11), 3065–3080.

Stiperski, I., Kavčič, I., Grisogono, B., & Durran, D. R. 2007. Including Coriolis effects in the Prandtl model for katabatic flow. *Q. J. Roy. Meteor. Soc.*, **133**(622), 101–106.

Zardi, D., & Whiteman, C. D. 2013. Diurnal mountain wind systems. *Pages 35–119 of:* Chow, F. K., De Wekker, S. F. J., & Snyder, B. (eds), *Mountain Weather Research and Forecasting*. Springer.